

1 Tsunami hazard in Lombok & Bali, Indonesia, due to the

2 Flores back-arc thrust

3

4 Raquel P. Felix¹, Judith A. Hubbard^{1,2}, Kyle E. Bradley^{1,2}, Karen H. Lythgoe², Linlin Li^{3,4} and
5 Adam D. Switzer^{1,2}

6 ¹Asian School of the Environment, Nanyang Technological University, Singapore

7 ²Earth Observatory of Singapore, Nanyang Technological University, Singapore

8 ³School of Earth Sciences and Engineering, Sun Yat-sen University, Zhuhai, China

9 ⁴Southern Marine Science and Engineering Guangdong Laboratory (Zhuhai), Zhuhai, China

10 Correspondence to: Raquel P. Felix (raquelpi001@e.ntu.edu.sg)

11

12 **Abstract.** The tsunami hazard posed by the Flores back-arc thrust, which runs along the northern coast of the
13 islands of Bali and Lombok, Indonesia, is poorly studied compared to the Sunda megathrust, situated ~250 km to
14 the south of the islands. However, the 2018 Lombok earthquake sequence demonstrated the seismic potential of
15 the western Flores Thrust when a fault ramp beneath the island of Lombok ruptured in two Mw 6.9 earthquakes.

16 Although the uplift in these events mostly occurred below land, the sequence still generated local tsunamis along
17 the northern coast of Lombok. Historical records show that the Flores fault system in the Lombok and Bali region
18 has generated at least six \geq M_s 6.5 tsunamigenic earthquakes since 1800 CE. Hence, it is important to assess the
19 possible tsunami hazard represented by this fault system. Here, we focus on the submarine fault segment located

20 between the islands of Lombok and Bali (below the Lombok Strait). We assess modeled tsunami patterns
21 generated by fault slip in six earthquake scenarios (slip of 1-5 m, representing Mw 7.2-7.9+), using deterministic
22 modelling, with a focus on impacts on the capital cities of Mataram, Lombok and Denpasar, Bali, which lie on
23 the coasts facing the strait. We use a geologically constrained earthquake model informed by the Lombok

24 earthquake sequence, together with a high-resolution bathymetry dataset developed by combining direct
25 measurements from GEBCO with sounding measurements from the official nautical charts for Indonesia. Our
26 results show that fault rupture in this region could trigger a tsunami reaching Mataram in <9 minutes and Denpasar

27 in ~23-27 minutes, with multiple waves. For an earthquake with 3-5 m of coseismic slip, Mataram and Denpasar
28 experience maximum wave heights of ~1.6-2.7 m and ~0.6 to 1.4 m, respectively. Furthermore, our earthquake
29 models indicate that both cities would experience coseismic subsidence of 20-40 cm, exacerbating their exposure

30 to both the tsunami and other coastal hazards. Overall, Mataram city is more exposed than Denpasar to high
31 tsunami waves arriving quickly from the fault source. To understand how a tsunami would affect Mataram, we
32 model the associated inundation using the 5m slip model and show that Mataram is inundated ~55-140 m inland
33 along the northern coast and ~230 m along the southern coast, with maximum flow depths of ~2-3 m. Our study

34 highlights that the early tsunami arrival in Mataram, Lombok gives little time for residents to evacuate. Raising
35 their awareness about the potential for locally generated tsunamis and the need for evacuation plans is important

36 to help them respond immediately after experiencing strong ground shaking.

37

Deleted: 1-2.5 m-high

Deleted: (Wibowo et al., 2021)

Deleted: ,

Deleted: (Lythgoe et al., 2021),

Deleted: 8

Deleted: 10-15

Deleted: 3

Deleted: 3.3

Deleted: 7

Deleted: 5

48 1 Introduction

49 Tsunamis sourced from back-arc thrust faulting, although not as common as megathrust tsunamis, could also
50 result in fatalities and severe damage and destruction to structures. Such are the cases for the Mw 7.7 1991 Limon,
51 Costa Rica (Suárez et al., 1995), Mw 7.9 1992 Flores Island, Indonesia, and Mw 7.5 1999 Ambrym Island of
52 Vanuatu (Regnier et al., 2003) earthquakes. Understanding the tsunami hazard associated with back-arc thrusting
53 is therefore important. Several studies have recognized the contribution of crustal earthquakes, which includes the
54 back-arc thrusting, in the development of tsunami hazard assessments (Selva et al., 2016; Grezio et al., 2017;
55 Behrens et al., 2021).

56
57 Here, we assess the deterministic tsunami hazard associated with the westernmost segment of the Flores Thrust,
58 a back-arc thrust that extends for >1,500 km, accommodating a portion of the convergence between the Indo-
59 Australian and Sunda Plates (Fig. 1a). Unlike its eastern segment, where the 1992 Mw 7.9 Flores Island earthquake
60 occurred, the western part of the fault has not hosted devastating tsunamis in recent years, although historical
61 records and previous studies show that it has generated at least eight tsunamigenic earthquakes (Fig.1b, NOAA
62 database, Hamzah et al., 2000; Rastogi and Jaiswal, 2006; Musson, 2012; Nguyen et al., 2015, Tsimopoulou et
63 al., 2020. The recent 2018 Lombok earthquake-triggered tsunamis were relatively minor because the earthquakes
64 mostly occurred beneath the island itself and not offshore; nevertheless, the occurrence of the 2018 Lombok
65 earthquakes gives new insights into the activity and geometry of this fault segment, and highlights the risk of
66 earthquakes and associated tsunamis along strike.

67

68 Our study focuses on the tsunami hazard caused by slip on the Flores Thrust in the Lombok Strait, a 20-60 km-
69 wide body of water between the islands of Lombok and Bali that connects the Java Sea to the Indian Ocean.
70 Because of its geometry, slip on the thrust in the Lombok Strait could generate tsunamis that would efficiently
71 propagate southwards and hit the west coast of Lombok and the east coast of Bali, where their capital cities
72 (Mataram and Denpasar) are located.

73

74 1.1 Regional setting

75 Bali and Lombok islands, east of Java, are part of the Lesser Sunda Islands (Fig. 1a). They are located along the
76 volcanic arc of the Java subduction zone, where the NNE-moving Indo-Australian Plate subducts beneath the
77 Sunda Plate (Dewey and Bird, 1970; Hamilton, 1979; Bowin et al., 1980; Silver et al., 1983, 1986; Hall and
78 Spakman, 2015; Koulali et al., 2016). The Java trench lies ~250 km to the south. The Flores back-arc thrust belt,
79 on the other hand, follows the northern edge of the islands. Here, the kinematics of fault slip and folding are
80 consistent with the sense of movement of the Indo-Australian Plate and associated shortening, indicating that the
81 Flores back-arc thrust also formed to accommodate stress associated with the plate collision (Silver et al., 1983,
82 1986).

83

84 The Flores back-arc thrust is an east-west-trending, south-dipping fault zone that extends for >1,500 km along
85 strike. It is composed of two main segments: the Wetar thrust zone to the east and the Flores Thrust to the west
86 (Silver et al., 1983, 1986); Fig. 1a). From east to west, the Flores Thrust traverses just north of central Flores,
87 Sumbawa, Lombok and Bali (Fig. 1a). From central Flores to east of Lombok, the thrust zone reaches to the

Formatted: Justified

Deleted: Most tsunami studies focus on earthquakes sourced by subduction zones, as they have high potential to generate destructive tsunamis (e.g., Mw 9.1 2004 Sumatra and Mw 9.0 2011 Tohoku earthquakes). Fewer studies focus on tsunamis generated by back-arc thrust faults within the upper plate that accommodate a component of plate convergence (Silver and Reed, 1988). The Mw 7.7 1991 Limon, Costa Rica (Suárez et al., 1995), Mw 7.9 1992 Flores Island, Indonesia, and Mw 7.5 1999 Ambrym Island of Vanuatu (Regnier et al., 2003) earthquakes demonstrated that back-arc thrusts can generate earthquakes and tsunamis resulting in fatalities and severe damage and destruction to structures. Hence, it is important to study the tsunami hazard associated with back-arc thrusting.

101 seafloor (Silver et al., 1983, 1986; Yang et al., 2020). As the deformation becomes blind from central Lombok to
102 the west, the thrust zone has been mapped based on folds visible in seismic reflection data, and also manifests as
103 a band of steeper north-facing slope on the seafloor (Silver et al., 1983; McCaffrey and Nabelek, 1987; Yang et
104 al., 2020). West of Bali, folds are fewer and have no to little seafloor expression (Silver et al., 1983; Fig. 1d),
105 suggesting that the Flores Thrust terminates at Bali (Yang et al., 2020). However, GPS measurements show that
106 the north-south convergence rate in Bali (5 ± 0.4 mm/yr) is similar to that onshore Java (6 ± 1 mm/yr), therefore
107 back-arc shortening may continue across a segment boundary along the Kendeng thrust in Java (Koulali et al.,
108 2016).

109

110 1.2 Seismicity of the Flores Thrust

111 Focal mechanisms show that from February 1976 to February 2021, the Flores Thrust generated 29 Mw 5.5 to 7.8
112 earthquakes within the upper 40 km of the crust (GCMT; Fig. 1a). Earthquakes in this region can be caused by
113 either tectonically driven fault slip or volcanic activity. In this back-arc region, most of the focal mechanisms are
114 characterized by east-west striking nodal planes with a fault plane dipping $26 \pm 8^\circ$ S; we infer that these are
115 associated with the Flores Thrust.

116

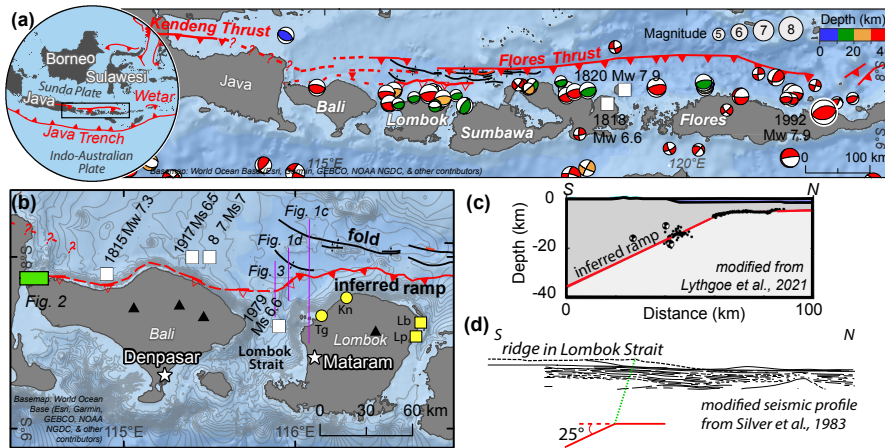
117 ~~The activity of this fault system is also testified by uplift recorded on its hanging wall.~~ From eastern Sumbawa
118 to central Flores, uplift is recorded by elevated terraces on the northern sides of the islands (Van Bemmelen,
119 1949). We suggest that the Quaternary reef terraces in northwest Bali (Boekschoten et al., 2000) are also related
120 to tectonic uplift above the Flores thrust system, suggesting that the fault extends all the way to the western
121 coast of the island (Fig. 2).

122

123 Although the earthquakes in this region are largely consistent with tectonic shortening, the active volcanoes not
124 only generate their own seismicity, but also play a role in the horizontal and vertical distribution of fault-generated
125 earthquakes (Lythgoe et al., 2021). A relationship between faulting and volcanic activity was observed for the
126 2018 Lombok earthquake sequence, which generated four $>Mw$ 6 events between 28th July to 19th August. These
127 earthquakes did not occur offshore on the northern frontal thrust of the Flores Thrust, but instead involved slip
128 along the deeper part of the fault and associated imbricate thrusts beneath Lombok, to the north of the active
129 Rinjani volcano (Salman et al., 2020; Yang et al., 2020; Lythgoe et al., 2021). While these earthquakes were not
130 directly caused by volcanic activity, the presence of the volcano constrained the earthquake distribution by
131 elevating the downdip limit of the seismogenic zone in the crust (Lythgoe et al., 2021). Based on relocated
132 earthquakes and seismic reflection data analysis, the earthquakes occurred on the Flores fault ramp, a blind thrust
133 dipping 25° S that flattens updip onto the Flores Thrust décollement at ~ 6 km depth (Lythgoe et al., 2021; Fig. 1c).

134

Deleted: This fault system has also produced uplift on its hanging wall



137

Figure 1: Regional setting of the Flores Thrust and its subsurface ramp-flat geometry. (a) Circle - The Flores back-arc thrust system, which is located along the northern edge of the Lesser Sunda Islands. The thrust is composed of two segments: the Wetar thrust to the east and the Flores Thrust to the west (black rectangle). Seismicity (USGS earthquake catalogue, 1976-2021) and focal mechanism solutions (GCMT, 1976-2021) show that the Flores Thrust is seismically active. The Mw 7.9 Flores Island tsunamigenic earthquake is the largest earthquake on record for this system and occurred at the eastern end of the thrust. (b) The western part of the Flores Thrust has generated historical tsunamigenic earthquakes (white rectangles; www.ngdc.noaa.gov; Hamzah et al., 2000; Rastogi and Jaiswal, 2006; Musson, 2012; Nguyen et al., 2015; Griffin et al., 2019). Yellow squares and circles: towns where a tsunami was reported following the Mw6.4 28th July and Mw6.9 5th Aug 2018 events, respectively. Tg – Tanjung, Kn – Kayangan, Lb – Labuhan Pandan and Lp – Leper. We interpret that the blind ramp mapped at Lombok (Lythgoe et al., 2021) extends westwards based on the seafloor morphology and uplifted terraces in the northwestern part of Bali (green rectangle; Fig. 2). Basemaps – World Ocean Base. **The map extent of (b) reflects the coverage of grid layer 1 (L1) used in the tsunami modelling. The basemap of (b) with only contour lines overlain is shown on Fig. S1.** (c) The geometry of the blind fault ramp is constrained by the seismicity of the 2018 Lombok earthquake sequence (Lythgoe et al., 2021). (d) Gentle folds interpreted by Silver et al., (1983) based on a seismic profile across the Lombok Strait. Below the profile we show our inferred location for the fault ramp.

Formatted: Font: 9 pt, Bold, Not Italic

Formatted: Font: (Default) Times New Roman, 9 pt

138

139 1.3 Tsunamigenic earthquakes of the Flores Thrust

140 Historical records (NOAA database, www.ngdc.noaa.gov) and tsunami studies (Hamzah et al., 2000; Rastogi and
 141 Jaiswal, 2006; Musson, 2012; Nguyen et al., 2015; Griffin et al., 2019) document at least four tsunamigenic
 142 earthquakes on the Flores Thrust, in addition to the two earthquakes in 2018, which produced local inundation
 143 (Fig. 1b). Three of these events occurred in the western part of the thrust zone, north of Bali. The oldest event on
 144 record is the 1815 Ms 7 earthquake, which triggered a landslide and tsunami; together, these events killed >1,200
 145 people. NOAA categorizes this as a probable tsunamigenic event, as it is unclear whether the tsunami was caused
 146 only by the coastal landslide, or by the earthquake and landslide together. The 1857 Ms 7 and 1917 Ms 6.5 events
 147 are described by NOAA as definite and probable tsunamigenic earthquakes, respectively. The 1857 event
 148 generated four consecutive tsunami waves, at least 3 m high, northwest of Flores Island (NOAA, 2021). In

149 addition, in the Lombok Strait, a 1979 Ms 6.6 tsunamigenic earthquake left 200 injured and killed 27 people,
150 although the tsunami is poorly documented and may have played a minor role in the destruction (Hamzah et al.,
151 2000).

152

153 The best-documented tsunamigenic earthquake on the Flores Thrust occurred in its far eastern part
154 (Yeh et al., 1993; Imamura and Kikuchi, 1994; Tsuji et al., 1995; Pranantyo et al., 2021). The 1992 Mw 7.9 Flores
155 Island earthquake injured 2,144 people and killed 2,080 (Yeh et al., 1993; Tsuji et al., 1995; Fig. 1a). This
156 earthquake occurred at ~16 km depth (Beckers and Lay, 1995), and generated a tsunami that propagated to the
157 northern coast of Flores Island within five minutes (Yeh et al., 1993). Field mapping shows that the tsunami
158 inundated the land as far as 600 m, with an average run-up height of ~2 to 5 m (elevation reached above sea level).
159 Anomalously high run-up heights of 20-26 m to the northeast may be associated with submarine landslides (Yeh
160 et al., 1993).

161

162 The recent 2018 Lombok earthquake sequence occurred primarily below land, but nevertheless small-scale
163 tsunamis were reported by the residents of northern Lombok (Tsimopoulou et al., 2020). When the Mw 6.4 July
164 event occurred, the northern coast of Lombok subsided by ≤ 0.1 m (Wibowo et al., 2021), and the northeastern
165 coast was hit by a tsunami at the towns of Labuhan Pandan and Tanjung, which were inundated 10-70 m with
166 run-up heights of ~1-2.5 m. For the Mw 6.9 August 5 event, although the northern coast was uplifted by ≤ 0.5 m
167 (Wibowo et al., 2021), the residents of the northwest towns, Tanjung and Kayangan, reported a tsunami that
168 inundated 7-40 m inland with a run-up height of ~1.7-2 m (Fig. 1b).

169

170 Together, these records show that the Flores Thrust is capable of generating significant thrust earthquakes with
171 associated land uplift/subsidence as well as local tsunamis. The full tsunamigenic potential of this fault system is
172 not known, as the observational window is short compared to typical earthquake recurrence intervals. [Here, the](#)
173 [observational window refers to the historical and seismic records. To our knowledge, there are no paleo-tsunami](#)
174 [studies in this area that are associated with the Flores Thrust. There is a paleo-deposit study in Bali, but it is](#)
175 [interpreted to be deposited by a tsunami generated by the megathrust rupture \(Sulaeman, 2018\). Hence, we rely](#)
176 [only on historical and seismic records when we refer to a short observational window. The tsunami studies related](#)
177 [to Flores Thrust are limited and they are about the numerical modelling of the historical tsunamis.](#) Here, we
178 explore what could happen when coseismic slip occurs on the Flores thrust ramp within the Lombok Strait, and
179 how the generated tsunami and coseismic land deformation would together affect the coastal cities of Mataram,
180 Lombok and Denpasar, Bali.

181

182

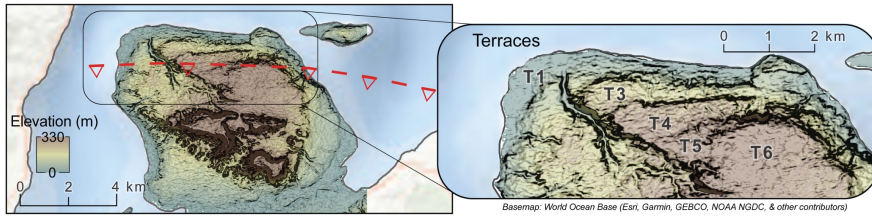


Figure 2: Six coastal terraces (T1-T6) identified using a digital elevation model (DEMNAS) in northwest Bali, likely uplifted due to slip on the Flores Thrust ramp. The location is shown as a green rectangle on the map in Figure 1b. Basemap – World Ocean Base.

184

185 1.4 Previous tsunami modelling studies

186 Tsunami modelling studies in this region commonly focus on the segment of the Sunda Megathrust along the
 187 Java trench (Okal and Borrero, 2011; Kurniawan and Laili, 2019; Suardana et al., 2019; Kardoso and Dewi, 2021)
 188 (Fig. 1a), with a few studies evaluating the western segment of the Flores Thrust (Løvholt et al., 2012; Rusli et
 189 al., 2012; Afif and Cipta, 2015), and four considering an earthquake sourced within the Lombok Strait (Rakowsky
 190 et al., 2013; Horspool et al., 2014; Pradjoko et al., 2018; Wibowo et al., 2021; Fig. 1b). All four studies show
 191 tsunami results in Mataram, Lombok; however, each study focuses on different aspects of tsunami modelling, and
 192 three predate the 2018 Lombok earthquake sequence, which illuminated important aspects of the fault geometry.
 193 The only study after the 2018 earthquakes (Wibowo et al., 2021) did not update their fault model to reflect new
 194 information about the geometry of the Flores Thrust derived from studies of the 2018 Lombok earthquake
 195 sequence. Overall, these prior results do not address the potential earthquake scenarios that we consider plausible:
 196 Rakowsky et al. (2013) study the sensitivity of inundation to land friction, Horspool et al. (2014) describe the
 197 probabilistic tsunami hazard, Pradjoko et al.(2018) considers a fault that is much too steep and uses bathymetry
 198 that is too coarse to produce reliable results, and Wibowo et al. (2021) did not consider the post-2018 earthquake
 199 studies of the fault geometry of the Flores Thrust.

200

201 Rakowsky et al. (2013) studied the sensitivity of inundation models in the region to the topography and friction
 202 parameters of the land surface. Their tsunami modeling was done using the ~900-m-resolution GEBCO dataset
 203 interpolated with measurements from ships and nautical charts; the interpolation method is not described in detail.

204 They considered a Mw 8.5 earthquake, and produced a maximum flow depth (vertical distance between the land
 205 and inundating water surface) of 10 m, with an inundation extent ranging from ~1-1.6 km in Mataram. This
 206 earthquake magnitude is larger than any observed event as the most recent estimates of the historical tsunamigenic
 207 earthquakes in the Flores Thrust ranges from Mw 6.6 to Mw 8.3, (Griffin et al., 2019), and that seismic records
 208 show that the 1992 Flores Island earthquake is Mw 7.9. They found that inundation distance depended on the
 209 topographic parameters: lower bottom friction or a bare earth digital terrain model produced higher inundation
 210 compared to higher friction or a digital surface model (with structures, e.g., houses). Their results highlight the
 211 importance of using an accurate surface model when assessing potential inundation.

212

Deleted: n unrealistically large

Deleted: ,

215 Horspool et al. (2014) focused on probabilistic tsunami hazard for all of Indonesia. They used a bathymetry dataset
216 that combined GEBCO data with measurements from Navy charts and multibeam surveys. ~~The maximum~~
217 ~~magnitude calculated for the Flores thrust is Mw 8.1, Mw 8.3 and Mw 8.5 for fault dips of 25-27°.~~ Their results
218 do not describe the regional hazard (e.g. wave heights, timing, inundation), but rather assess how much of the
219 local hazard is contributed by this fault system rather than the megathrust. They showed that ~~for a 500-year return~~
220 ~~period, the tsunami hazard in Mataram is 10-30% most likely due to the shallow part of the Flores Thrust.~~

Deleted: For the western Flores thrust,

Deleted: they set 1 m of slip on a range of 25-27°-dipping, 10x20 km sub faults (equivalent to a Mw6.4 earthquake) within the 3-30 km seismogenic depth of the Lombok Strait

221 ~~▼~~
222 Pradjoko et al. (2018) used a model of a Mw 6.4 earthquake to simulate a scenario similar to the 1979 event,
223 which was the largest recorded earthquake in this region prior to the 2018 Lombok earthquake sequence. They set
224 2.5 m of fault slip on a 72°-dipping fault (significantly steeper than the 25° dip we interpret for the fault) centered
225 at 25 km depth. Using GEBCO bathymetry to model tsunami propagation (with a coarse horizontal resolution of
226 ~900 m), their results indicate that a Mw6.4 earthquake could generate a 0.13-0.2 m-high tsunami wave that
227 arrives at the coast of Mataram ~18-20 minutes after the earthquake.

Deleted: given an arbitrary 500-year return period on the fault, 10-30% of the tsunami hazard in Mataram is due to the shallow part of the Flores Thrust. ¶

228
229 The study by Wibowo et al. (2021) focused on the tsunami hazard posed by a Mw 7.4 earthquake on the Flores
230 thrust to the northern coasts of Lombok and Bali. They set 2.7 of slip on a 27°-dipping fault plane with dimensions
231 of 75 km x 27 km centered at 27 km depth. The fault parameters they used are based on the mean values of the
232 earthquake sources in the USGS 1900-2020 earthquake database. The orientation and depth of the fault are similar
233 to those we use in our modeling, but the updip tip of the fault in their model is located about 25 km north of the
234 islands rather than along the northern coast of the islands, as we interpret from the 2018 Lombok earthquake
235 sequence and bathymetry in the Strait. They used the 180-m resolution National Bathymetry of Indonesia
236 (BATNAS) dataset as input bathymetry in the numerical simulations. Their focus was on the impact along the
237 northern coasts, but they note that the tsunami arrives in Mataram and Denpasar in 9 and 25 minutes, respectively.
238 They also find that the maximum wave height is 1.5 m in Mataram and 1 m in Denpasar.

239
240 Following the 2018 Lombok earthquake sequence, we now have a more accurate understanding of the location
241 and subsurface geometry of the Flores Thrust in this region. Hence, the earthquake models we use in our study
242 are geologically well-constrained. In addition, since tsunami propagation in shallow water depends strongly on
243 the bathymetry, we develop and incorporate a new bathymetric model by combining the GEBCO dataset with
244 sounding measurements from the official nautical chart for Indonesia. This is particularly important along the
245 shallow coast, where seafloor roughness has a strong control on wave propagation. In our study, we show the
246 tsunami results from six different earthquake scenarios within the Lombok Strait, highlighting impacts on the
247 populated capital cities of Mataram, Lombok and Denpasar, Bali, as both cities face the Strait. We also calculate
248 the coseismic uplift and subsidence for varying slip amounts, and report this together with the tsunami time history
249 and pattern and the maximum wave height. An inundation scenario is also included for the city of Mataram.

2151 **2 Methodology**

2152 **2.1 Fault model setup**

2153 The 2018 Lombok earthquake sequence illuminated the geometry of the Flores Thrust beneath Lombok (Fig. 1c).
2154 Together, relocated aftershocks, earthquake slip distributions, and seismic reflection imaging indicate a blind fault

262 ramp dipping 25°S that flattens updip to a décollement at ~6 km depth and continues north below the Bali Sea.
 263 The part of the thrust ramp that ruptured in the 2018 sequence extends 45 km downdip and 116 km lengthwise
 264 (Lythgoe et al., 2021; Fig. 1c & 3).

Deleted:

265 We use these fault parameters to set up our fault model, choosing a fault with an east-west strike, similar to the
 266 general trend of the Flores Thrust, positioned across the Lombok Strait. The complete parameters are listed in
 267 Table 1. We are not trying to replicate the 2018 earthquakes, but rather consider an earthquake on the neighboring
 268 part of the fault that did not rupture in that sequence. The eastern boundary of the fault model slightly overlaps
 269 with the western limit of the 2018 earthquake sequence. Such overlapping ruptures have been observed in Kuril
 270 Trench (Ammon et al., 2008) and Peru-Chile Trench (Bilek, 2010). We extend the western edge of the model to
 271 below the eastern edge of Bali, in order to span the width of the Strait; the fault likely continues further west (as
 272 evidenced by uplifted terraces and seismicity), but rupture to the west would occur below land and would not
 273 contribute to a tsunami. As there are limited available information on the structural geology and the seismicity of
 274 the Flores Thrust in this region, While there is limited data within the strait to assess the continuity of the fault,
 275 there is no reason to believe that there are significant structural variations along strike. The focal mechanisms for
 276 the events near Bali have very similar strike and dip to that at Lombok (Fig. 1a). When varying the fault dips to
 277 18° and 34°, representing the minimum and the maximum limits of the fault dip uncertainty, they have minimal
 278 impact on the tsunami model. The tsunami energies inherent in these two models are only 5-8% different from
 279 the energy of our model with a 25° fault dip (Felix et al., 2021). Hence, minor structural variations would result
 280 in minor changes in arrival times and wave heights but would not be likely to have a strong effect on our results.

Deleted: with

281 **Table 1: Parameters of fault models A and B used in the numerical modelling.**

Parameters	Fault model A	Fault model B
Epicenter longitude	115.77° E	115.77° E
Epicenter latitude	8.3821° S	8.2905° S
Focal depth	15.5 km	10.8 km
Width	45 km	22.5 km
Length	116 km	
Strike	90° E	
Dip	25° S	
Rake	90°	

Deleted: The eastern boundary of the fault is defined by the western limit of the 2018 earthquake sequence. We extend the western edge of the model to below the eastern edge of Bali, in order to span the width of the Strait; the fault likely continues further west (as evidenced by uplifted terraces and seismicity), but rupture to the west would occur below land and would not contribute to a tsunami.

Formatted: Font: Times New Roman, 10 pt

Formatted: Centred

Formatted Table

Formatted: Font: Times New Roman, 10 pt

Formatted: Centred

Formatted: Font: Times New Roman, 10 pt

Formatted: Centred

Formatted: Font: Times New Roman, 10 pt

Formatted: Centred

Formatted: Font: Times New Roman, 10 pt

Formatted: Centred

Formatted: Font: Times New Roman, 10 pt

Formatted: Centred

Formatted: Font: Times New Roman, 10 pt

Formatted: Font: Times New Roman, 10 pt

Formatted: Centred

Formatted: Font: Times New Roman, 10 pt

Formatted: Font: Times New Roman, 10 pt

Formatted: Centred

Formatted: Font: Times New Roman, 10 pt

Formatted: Centred

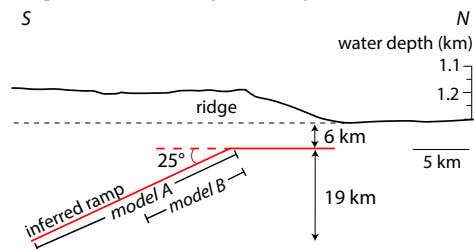
282

283 We trace the upper blind tip of the fault ramp following the southern edge of a north-facing seafloor slope. This
 284 surface morphology coincides with folding interpreted from seismic reflection surveys (Silver et al., 1983; Yang
 285 et al., 2020), and we interpret that the folding formed due to slip across a bend at the upper tip of the blind fault
 286 ramp (Fig. 1b). We extend the fault ramp to a depth of 25 km below the seafloor, which represents the maximum
 287 seismogenic depth in this region based on historical seismic records and the maximum depth of seismicity
 288 observed in the 2018 sequence (Lythgoe et al., 2021).

289 We model two fault ruptures on this fault (Models A and B, Fig. 3). Model A consists of a whole-fault rupture,
 290 while Model B allows only the upper half of the ramp to slip. This second model represents a scenario similar to

Formatted: Centred

300 the 2018 Lombok earthquakes, where most of the slip occurred on the shallow part of the fault ramp. However,
 301 the maximum rupture depth at Lombok was interpreted to be limited by the elevated geothermal gradient
 302 associated with the volcano. In the Lombok Strait, there is no such volcano; thus, it is likely that slip within the
 303 Lombok Strait could reach deeper due to the colder geothermal gradient.



304

Figure 3: Profile of the fault geometry used in the tsunami modelling relative to the seafloor ridge. We study two fault slip models: model A (whole-ramp rupture) and model B (slip only on the upper half of the ramp). The location of the profile is shown in Fig. 1b.

305 2.2. Slip model

306 For both Models A and B, we consider three deterministic scenarios with uniform slip of 1, 3, and 5 m (six
 307 scenarios total). The modeled historical tsunamigenic earthquakes in the Flores Thrust are estimated to have
 308 magnitudes ranging from Mw 6.7 to Mw 8.5 (NOAA, Musson et al., 2019; Griffin et al., 2019). Using the
 309 scaling relationship for magnitude and slip of shallow crustal reverse faulting by Thingbaijam et al. (2017),
 310 these earthquake magnitudes have average slip ranging from 1 to 5 m. In order to represent this range, we use
 311 the minimum (1 m), the mid-range (3 m) and the maximum (5 m) slip values in our modelling. In the
 312 subsequent texts, we refer to these slip models as A-1, A-3 and A-5 for fault model A and B-1, B-3 and B-5 for
 313 fault model B. We note that although modelling with more complex rupture scenarios would perhaps be a more
 314 detailed option (e.g. Serra et al., 2021), the current information that we have about the Flores Thrust in Bali and
 315 Lombok region, however, is limited. Hence, we think that it is better to use a planar fault model and uniform
 316 slip to lessen the use of random parameters that could increase the uncertainty in the results. We also note that
 317 although probabilistic approaches are becoming more common, the deterministic method is still included in
 318 recent tsunami hazard studies (e.g. Wronna et al., 2015; Roshan et al., 2016; Gonzales, et al., 2019; Escobar et
 319 al., 2020; Rashidi et al., 2020; Hussain et al. 2021; Rashidi et al., 2022).

320 In order to focus on the impact of tsunami generation, we include only slip on the fault ramp (no slip transferred
 321 onto the northern décollement). This updip termination of slip was observed in the Lombok sequence (Lythgoe et
 322 al., 2021) and is therefore realistic in our region to the west as well. Although we consider uniform slip, earthquake
 323 slip is known to be spatially variable, and in particular to taper around the edges of the slip patch. We evaluate the
 324 impact of this taper on the initial seafloor deformation using the Green's function for rectangular dislocations
 325 (Okada, 1992) in the code Unicycle (Moore et al., 2019); we find that tapering the slip slightly modifies the uplift
 326 profile by broadening it and shifting it to the south (downdip direction) but does not significantly change the
 327 model (Fig. 4).

Deleted: 1

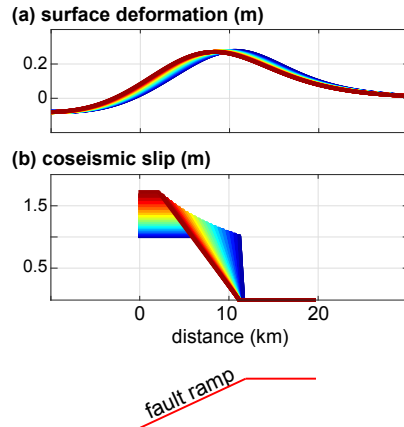
Formatted: Left

Deleted:

Field Code Changed

Deleted: (

331



332

333 **Figure 4: Influence of tapering the updip slip on seafloor deformation. The maximum slip varies across the models in**
 334 **order to preserve the mean slip. (a) The seafloor deformation profiles have similar amplitudes and shapes with slightly**
 335 **offset peaks, even for very significant tapers. (b) Different slip tapers considered. A more gradual taper (red shades)**
 336 **shifts the peak uplift in the downdip direction of the fault ramp. A more abrupt slip taper (blue shades) shifts the peak**
 337 **uplift towards the upper fault bend.**

338 To better translate the models into equivalent earthquakes, we calculate the equivalent Moment Magnitude (M_w)
 339 for each modeled event, using a rigidity of 35 GPa and 30 GPa for models A and B, respectively. These are the
 340 mean rigidities calculated from the values presented in Sallarès and Ranero (2019) and Sallarès et al. (2021),
 341 every 1 km interval from 6 to 25 km depths for Model A, and from 6 km to 15.5 km depth for model B. Since
 342 Model A has a wider fault surface, for the same amount of slip, it produces larger magnitudes compared to Model
 343 B (Table 2). In each model, we consider only the part of the fault that lies below the Lombok Strait, since this is
 344 the part of the fault that is submarine and therefore capable of generating tsunamis. We note that an earthquake
 345 rupturing this fault segment could involve slip further along strike, either to the west (below Bali) or to the east
 346 (below Lombok, although this part of the fault recently ruptured in multiple earthquakes and is relatively less
 347 likely to slip again). Indeed, reaching 5 m of slip within the Lombok Strait alone would likely require a longer
 348 rupture, and therefore a larger magnitude than the values reported in Table 2, given known scaling relationships
 349 between fault area and coseismic slip (Thingbaijam et al., 2017).

350 **Table 2: Equivalent Moment Magnitudes (M_w) for Models A and B for a given slip amount. Model A**
 351 **ruptures the full ramp while Model B ruptures only the upper half of the ramp. Both models have a fault**
 352 **length of 116 km. The magnitudes here are minima, as each of these events could also include slip on the**
 353 **along-strike part of the fault.**

354

	Model A	Model B
▲	Fault width: 45 km	Fault width: 22.5 km
▲		

Deleted: (
 Deleted: ,
 Deleted: ;
 Deleted: ,
 Deleted: standard rigidity of 30 GPa.
 Deleted: 1

Deleted: 1
 Deleted: (Wells and Coppersmith, 1994; Hanks, 2002; Biasi and Weldon, 2006; Hanks and Bakun, 2008).

Deleted: 1

Formatted: Font: Bold
 Formatted: Font: 10 pt, Bold
 Formatted Table
 Formatted: Font: Bold

Slip (m)	Mw	
1	7.5	7.2
3	7.8	7.5
5	7.9	7.7

Formatted: Font: Bold

Deleted: 4

Deleted: 7

Deleted: 2

365

366 2.3 Bathymetry

367 Accurate modeling of tsunami wave propagation requires a high-resolution bathymetric map, especially in shallow
 368 water. By using detailed bathymetry together with a fine grid size, modelled simulations of tsunami wave heights
 369 have been shown to effectively match real near-coast waveforms (Satake, 1995). However, in many parts of the
 370 world, high resolution bathymetric data are unavailable. In general, regional tsunami studies use only one
 371 bathymetric dataset (e.g., Satake, 1988), commonly either ETOPO (<https://www.ngdc.noaa.gov/mgg/global/>) or
 372 GEBCO (<https://www.gebco.net/>), because they are publicly available and have wide coverage. However, these
 373 datasets have an artificially smooth seafloor (Marks and Smith, 2006), especially at shallow depths, because of
 374 the low density of interpolated points (e.g., Fig. 5). In local tsunami studies, the detailed seafloor morphology in
 375 shallow water is critical, since seafloor roughness in these regions has nonlinear effects on wave propagation
 376 (Wang and Power, 2011). Kulikov et al. (2016) demonstrated that tsunami propagation modeled using the GEBCO
 377 dataset results in substantial errors in the estimation of wave propagation.

378

379 We generate a high-resolution bathymetric model of the region of interest by combining water depth
 380 measurements from GEBCO with sounding measurements from the official nautical charts of Indonesia
 381 (<http://hdc.pushidrosal.id/>). The publicly available GEBCO dataset is provided as an interpolated raster, but also
 382 includes the original data points used for interpolation. These data points (water depths) are derived from a variety
 383 of sources, both direct (echo soundings, seismic reflection, isolated soundings, electronic navigation chart
 384 soundings) and indirect (e.g. satellite altimetry, flight-derived gravity data). Using the Type-Identifier Grid file
 385 from GEBCO, which includes the source of the depth data, we identify and extract only the water depths acquired
 386 by direct measurement (Fig. 5).

387

388 The GEBCO data in this region are concentrated along the heavily-travelled ship tracks between the islands of
 389 Bali and Lombok, and are too low resolution near the coasts to accurately model tsunami propagation and wave
 390 heights (Fig. 5a). We improve the resolution of our bathymetry by digitizing sounding data from the official
 391 nautical charts of Indonesia, which are densest in the coastal regions near the cities of Denpasar (Bali) and
 392 Mataram (Lombok) and therefore critical for modeling near-shore wave heights in these regions (Fig 5b). We also
 393 trace the coastline using the National Digital Elevation Model (DEMNAS, <http://tides.big.go.id/DEMNAS/>), and
 394 cross check it using satellite images from Esri World Imagery (<https://www.arcgis.com/>).

395

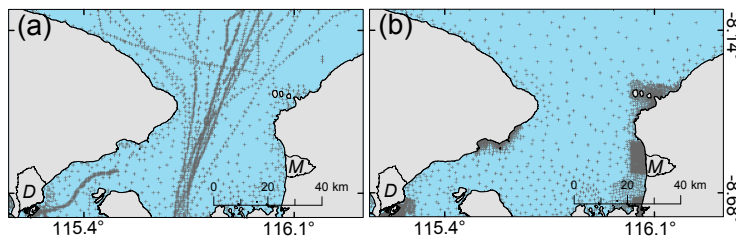
396 We combine the water depth measurements from both sources and the coastlines into a single dataset, and then
 397 interpolate the data using the 'Topo to Raster' tool in ArcGIS. This tool is based on the ANUDEM program
 398 developed by Hutchinson (1989), and generates a continuous digital elevation model based on point data that
 399 takes into account the hydrological correctness of the resulting raster. While this method was developed on the
 400 basis of subaerial water flow, it has also been used to effectively generate bathymetries for tsunami studies in

404 other regions (Fraser et al., 2014; Darmawan et al., 2020; Wilson and Power, 2020). We note that the shallow
405 shelf regions of the Lombok Strait were likely incised subaerially during the late Holocene sea-level drop
406 (Boekschoten et al., 2000), and their morphologies therefore likely reflect subaerial water flow processes.

407

408 We set the resolution of our interpolated raster to 30 m, as this is similar to the mean distance between the data
409 points along the coasts of Mataram (~27) and Denpasar (~36 m). Our final bathymetry represents a reasonable
410 balance between achievable accuracy at shallow depths and computational efficiency. We validate the interpolated
411 bathymetry by comparing its values with the source data; the mean difference in the shallow regions offshore
412 Mataram and Denpasar is <0.4 m.

413



414

415 **Figure 5: Comparison of the point density of water depth measurements from (a) GEBCO (direct measurements) and**
416 **(b) nautical charts (soundings). GEBCO data are densest along the center of the Lombok Strait (following ship tracks),**
417 **while the nautical chart soundings are concentrated near the coastal cities. Combining these data points enhances the**
418 **accuracy of the resulting bathymetry (shown in Fig. 6). Crosses – locations of measurements. Polygons on land – cities**
419 **of Denpasar, Bali and Mataram, Lombok. D = Denpasar, M = Mataram.**

420

2.4 Topography in Mataram, Lombok

Deleted: 3

421 Based on our tsunami model runs, the highest wave heights are observed along the coast of Mataram, Lombok.
422 In order to further explore the tsunami hazard in this populated area (Fig. 6), we model the inundation of the
423 onshore region. The inundation distance and run-up height of a tsunami can vary significantly depending on
424 factors such as the average slope of the coast and the land cover roughness (Kaiser et al., 2011; Griffin et al.,
425 2015); an accurate forecast requires a high-resolution Digital Surface Model (DSM) that maps the buildings and
426 trees.

427

428 We use a Digital Surface Model generated by Apollo Mapping based on Pleiades satellite imagery. The DSM has
429 a horizontal resolution of 1.5 m and a vertical error of ± 3 m. This vertical error is the lowest possible for digital
430 elevation models without ground control points, which we do not have access to. We use a DSM rather than a
431 DTM (Digital Terrain Model) to better represent the man-made structures (e.g., houses, infrastructure) present in
432 Mataram city. There are a few areas where the DSM is unavailable along the coast, due to difficulties in data
433 processing associated with tides. We fill these areas with 1.5-m resampled elevation data from DEMNAS, the
434 national elevation model for Indonesia, which has a coarser original horizontal resolution of 8 m. The vertical
435 datum of the merged data is referenced to EGM2008.

436

437 In order to run the inundation modelling, the topographic data must be merged with the bathymetry so that the
438 incoming wave can be smoothly modeled across the sea-land interface. To match the resolution of the DEMNAS-
439 DSM model, we generate another bathymetry model with 1.5 m resolution in the Mataram region using the same
440 'Topo to Raster' interpolation method as used previously for the bathymetry. We match the coastlines of the two
441 datasets to generate the final combined model.
442

443 2.5 Tsunami modelling using COMCOT

444 We model the tsunami generation, propagation, run-up and inundation using the Cornell Multi-grid Coupled
445 Tsunami (COMCOT) model developed by Liu et al. (1995). This modeling system solves linear and nonlinear
446 shallow water equations using a modified leap-frog finite difference approach (Wang & Power, 2011). It uses a
447 nested-grid layer algorithm to increase its computational efficiency. The Okada (1985) model is used to calculate
448 surface deformation due to fault slip. We use this model in our study as it has been extensively adopted and
449 validated for modelling tsunami events (e.g., 1960 Mw 9.5 Chilean tsunami – Liu et al. 1995; 2004 Mw 9 Indian
450 Ocean Tsunami - Wang and Liu, 2007; 2006 Mw 7.7 South Java tsunami – Tri Laksono et al. 2020; 2010 Mw 7.8
451 Mentawai earthquake – Hill et al. 2012; 2011 Tohoku tsunami – Chau and Lam, 2015).
452

453 For our tsunami modelling, we set up a total of six grid layers in a spherical coordinate system, with finer
454 resolution in the shallow regions along the coasts of Mataram and Denpasar (Fig. 6). For the parent grid layer
455 (L1), the extent covers the entire islands of Bali and Lombok (shown as the extent of Fig. 1b) and its grid size is
456 set to 150 m. We use 3 nested grid layers in Mataram with resolutions of 30 m (L2), 6 m (L3) and 1.5 m (L4, Fig.
457 6), while we use 1 sublayer in Denpasar with a grid size of 30 m (L5, Fig. 6). We added a 1.5 m grid size resolution
458 in Mataram to simulate the inundation of model A-5, representing the “worst case” of our various models. This
459 does not necessarily mean that it gives the worst-case tsunami scenario, and that a lower magnitude earthquake
460 can generate a comparable tsunami (Salaree et al., 2021). We only use one earthquake scenario because high
461 resolution inundation modeling is computationally expensive. Linear and nonlinear shallow water equations are
462 used on L1 and L2-L5, respectively. We set the Manning’s roughness coefficient in L3-L5 to 0.013 on the water
463 region, and 0.03 on land (Wang and Power, 2011). The results of the simulations in grid layer L1 are shown on
464 Figures 7 and 8, and the results in L2 and L5 are shown on Figures 9-11. The simulations in L4 are shown as
465 inundation maps on Figures 12 and 13.
466

467 We run the tsunami simulation from the time of the earthquake for one hour; this is sufficient to capture both the
468 first wave and a series of smaller, later waves, since the coastal regions we are interested in are close to the source
469 (<100 km). To observe the tsunami arrival pattern along the coasts of Mataram and Denpasar within the hour, we
470 select virtual tide gauge locations along the 10-m bathymetric contour, facing the coastal areas where dense man-
471 made structures are identified from satellite images. The results of the tsunami modeling are illustrated using maps
472 of the initial sea surface deformation, maximum wave height, coseismic land subsidence in Bali and Lombok,
473 time series of wave arrivals at the virtual tide gauges, and maps of inundation depth in Mataram.
474
475

Deleted: 4

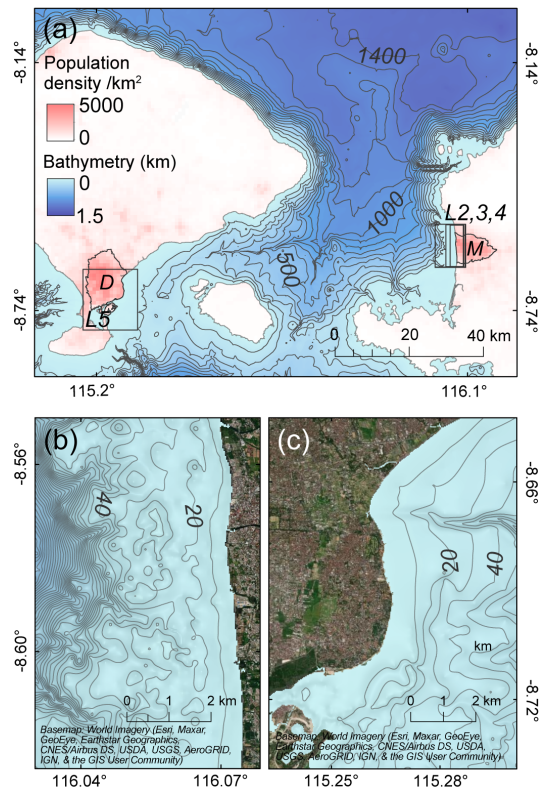
Deleted:

Formatted: English (US)

Formatted: Normal

Formatted

Deleted: For our tsunami modelling, we set up five nested-grid layers in a spherical coordinate system, with finer resolution in the shallow regions along the coasts of Mataram and Denpasar (Fig. 6). The recommended grid size ratio is 3 to 5 (Wang and Power 2011), and we want to use a 30 m resolution layer along the coasts of Mataram (layer 2, Fig. 6) and Lombok (layer 5, Fig. 6). We therefore set the grid size of the main parent layer 1 to 150 m (Wang and Power, 2011). We create two more sub layers (3 & 4) near Mataram to generate a 1.5 m grid size to model the inundation. High resolution inundation modeling is computationally expensive, so we only simulate inundation in Mataram for one earthquake scenario: 5 m slip on fault model A (full width). This represents the “worst case” of our various models. In this modeling, we use the linear shallow water equation in grid layer 1, as it covers the deeper water region, and the nonlinear equation in grid layers 3 to 5, which target the shallow depths, to incorporate the effect of bottom friction. A Manning’s roughness coefficient of 0.013 is used for the water region, and 0.03 on land (Wang & Power, 2011). ¶



498

Figure 6: The generated bathymetry in the Lombok Strait. (a) The bathymetry has a north-south trending ridge along a narrow path between Bali and Lombok with its base at 1.4 km water depth, which is the deepest water depth in this region. The extent of (a) matches the extent of grid layer L1 used in the tsunami modelling. The finer grid layers L2-L4 and L5 are focused on the populated cities of Mataram and Denpasar, respectively. M = Mataram, D = Denpasar. **Grid resolutions: L1 = 150 m; L2 and L5 = 30 m; L3 = 6 m, and L4 = 1.5 m.** The population density is from worldpop.org (Bondarenko et al., 2020). (b) The linear coast of Mataram faces a rugged but gently dipping seafloor that suddenly steepens ~3-4 km from the coast. (c) Denpasar city has a more complex coastline and a smoother seafloor. Basemaps – World Imagery.

Deleted:

499 3 Results

500 3.1 Cosismic deformation and maximum wave height

501 When slip occurs on the Flores Thrust ramp during an earthquake, the elastic response of the crust will lead to
 502 broad changes in the elevation of the ground surface. In the north, above the fault ramp, the seafloor will rise
 503 (uplifting any ocean column above), whereas the southern region will subside (Fig. 7a-c). Associated with this
 504 process, the islands of Bali and Lombok will tilt towards the south (Fig. 7a-c, 8a-c). As the initial sea surface

505 deformation will have the same magnitude as the land deformation, the initial wave will be unnoticeable relative
506 to the coast, which experiences the same vertical motion (Fig. 7d-f, 8d-f). As the fault patches of our fault models
507 A (45 km) and B (22.5 km) are much larger than the ~1.4 km maximum water depth in Lombok Strait, we note
508 that the dispersion effect due to the water column (Kajiura, 1963) is not included here. The energy transmitted to
509 the sea surface from the seafloor by our models is only 2-3% different from the filtered versions (Felix, et. al.,
510 2021).The initial waves in our models correspond to tsunami energies of 1, 13, and 36 TJ for Model A and 1, 7,
511 and 20 TJ for Model B for 1, 3, and 5 m of slip, respectively (Felix et al., 2021).

Deleted: ¶

512 The coseismic land change and tsunami heights are influenced by the distance from the fault and the shape of the
513 coastline. Lombok and Bali have east-west trending headlands at 8.38°S latitude. In Lombok, the less protruding
514 headland connects southwards to a north-south-trending linear coastline. In Bali, on the other hand, the headland
515 protrudes further and connects to a southeast-facing coastline with a curved morphology. When the full fault slips
516 (model A), the northern half of the islands, including the headlands at 8.38°S, are uplifted (Fig. 7). This uplift acts
517 to counter any transient waves, including the initial wave, and results in a maximum relative wave height of
518 generally <0.5 m along the northern coasts. The exception is the headlands, where the waves can be much higher;
519 here, the waves refract towards the concave coastlines, and the wave heights can reach ~1.9 m high for models
520 A-3 and A-5 (Fig. 7d-e).

Deleted: (Fig. 7).

Deleted: -0.6

Formatted: Not Highlight

Formatted: Not Highlight

Deleted: 7

Deleted: 3-5 m of coseismic slip

Deleted: 5 m of fault slip

Deleted:

Deleted: 3 m slip

Deleted: 1 m slip

Deleted: 6-

Formatted: Not Highlight

Deleted: 3-5 m of coseismic slip

Deleted: 0

Formatted: Not Highlight

Deleted: .7

Deleted: ¶

Deleted: 1.5

Formatted: Not Highlight

Deleted: 3-5 m of coseismic slip

Formatted: Not Highlight

Deleted: 5

Formatted: Not Highlight

Formatted: Not Highlight

Deleted: 5

Formatted: Not Highlight

Deleted: to

Deleted: 3-5 m

Deleted: of coseismic slip

Deleted: ¶

521 Along the southern coasts, on the other hand, coseismic subsidence acts to increase the relative tsunami heights.
522 The subsidence in southern Lombok and Bali can reach as high as ~0.3-0.4 m for model A-5, ~0.1-0.25 m for
523 model A-3, and <0.1 m for model A-1. We find that overall, the west coast of Lombok experiences higher tsunamis
524 than the southeast coast of Bali, because it is closer to the tsunami source and the coastline is perpendicular to the
525 source, making it more exposed to the propagating waves. The maximum tsunami height on the west coast of
526 Lombok is ~1.8-3.7 m for models A-3 and A-5. On the other hand, the more distant and better protected
527 southeastern coast of Bali has a maximum wave height of ~1.3-2.2 m given the same slip amount, with slightly
528 higher waves within the semi-enclosed bays (Figs. 7d-e).

529 When only the upper half of the fault ramp slips (model B), the uplift patch is narrower and the subsidence region
530 is broader, covering about three quarters of the coasts of Lombok and Bali. Unlike in model A, the headlands at
531 8.38°S are now within the area of subsidence (Fig. 8). This results in an increase in the relative maximum wave
532 height at the headlands, with ~2-4 m high tsunamis for models B-3 and B-5 (Fig. 8d-e). Similarly, the west coast
533 of Lombok is hit by ~1.7-3.4 m high tsunamis, while southeastern Bali experiences ~0.8-2 m high tsunamis for
534 models B-3 and B-5.

535 The two fault models generate similar maximum wave heights along the west coast of Lombok (Fig. 9), while the
536 tsunamis generated by model A are slightly higher than model B along the southeastern coast of Bali (Fig. 10). In
537 both models, however, we consistently observe higher tsunami waves in Lombok compared to Bali. This
538 difference is best observed using the virtual tide gauge records situated near the cities of Mataram and Denpasar.

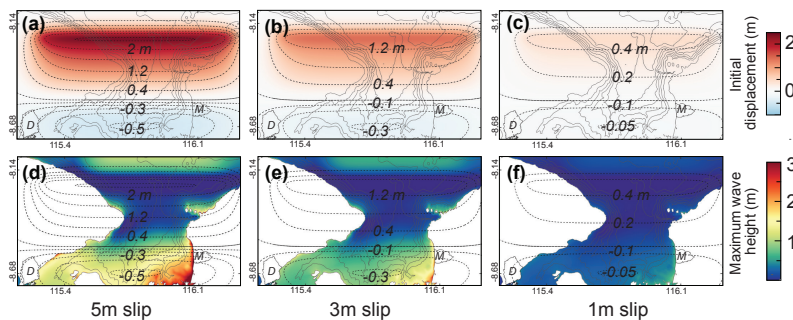
539

540 3.2 Tsunami time series in Mataram, Lombok and Denpasar, Bali

563 The tide gauge records show that the tsunami arrival times in Mataram and Denpasar are insensitive to the fault
 564 model geometries that we consider. The first and highest wave in Mataram arrives ~~<9~~ minutes after the earthquake
 565 and it reaches its peak at ~11 minutes, followed by a drawdown at ~15-17 minutes. Three more waves reach the
 566 coast at ~20, ~35 and 45 minutes (1st row, Fig. 11). The first wave in Mataram is ~2.5-2.7 m high for 5 m slip (A-
 567 5 & B-5), ~1.6-1.7 m high for 3 m slip (A-3 & B-3), and ≤ 0.6 m high for 1 m slip (A-1 & B-1) (Figs. 9 & 11).
 568 The height of the second wave is ~1.9-2.5 m, ~1.2-1.5 m, ~0.4-0.5 m, respectively, for 5 m, 3 m, and 1 m slip.
 569 The third wave is ~0.6-0.7 m high for a 5 m slip, ~0.3-0.4 m for a 3 m slip, ~0.2-0.3 m for 1 m slip. The last wave
 570 is ~0.1-1.3, ~0.6-1, and ≤ 0.2 m, respectively, for 5, 3, and 1 m slips.

571 In Denpasar, the waves are smaller and take longer to arrive (2nd row, Fig. 11). For fault model A, the first wave
 572 arrives at ~12-18 minutes and reaches its peak at ~30 minutes. It is followed by a drawdown at ~38 minutes and
 573 a second wave at ~48-53 minutes. Fault model B has a similar wave pattern with model A, however, its wave
 574 arrival times are slightly later. The first wave in model B arrives at ~23-27 minutes, followed by a drawdown at
 575 ~40 minutes and a second wave at ~52-55 minutes (Fig. 11). As Denpasar is further from the tsunami source and
 576 has a complex coastline, its wave records are not as uniform as those along the linear coast of Mataram. For both
 577 fault models A and B, relatively higher tsunami waves are generated within the semi-enclosed bay in the northeast
 578 of Denpasar, while lower waves reach southwestwards along the concave coastline (Fig. 10; Gauge 4 on Fig. 11).
 579 Although they have a similar trend, the wave heights generated by model A are slightly higher than model B. For
 580 model A, the maximum wave heights generated are ~1.4 m (A-5), ~0.9 m (A-3) and ~0.3 m (A-1). For model B, the
 581 maximum wave heights generated are ~0.8 m (B-5), ~0.6 m (B-3) and ≤ 0.2 m (B-1) (Fig. 11).

582
583



584
 Figure 7: Initial surface deformation and maximum wave heights in 1 hr generated by different slip amounts on the
 full 45-km wide fault ramp (model A). Upper panels (a-c): The coseismic deformation generated by (a) 5 m, (b) 3 m,
 and (c) 1 m fault slip events result in uplift in the northern half of the islands and subsidence in the south. Lower panels
 (d-f): Maximum sea surface displacements for (d) 5 m, (e) 3 m, and (f) 1 m fault slip events. Maps are adjusted to show
 wave heights relative to the post-earthquake land surface rather than initial sea level by subtracting the coseismic
 displacement (dashed contour lines). The west coast of Lombok is hit by higher tsunami waves than the southeastern
 coast of Bali. Polygons on land – cities of Denpasar, Bali and Mataram, Lombok. D = Denpasar, M = Mataram.

585

Deleted: <8

Deleted: 8

Formatted: Superscript

Deleted: 2

Deleted: 4

Deleted: 4

Deleted: 3

Deleted: 1

Deleted: 2

Deleted: 6

Deleted: 1

Deleted: 7-0.9

Deleted: 3-0.5

Deleted: ¶

Formatted: Not Highlight

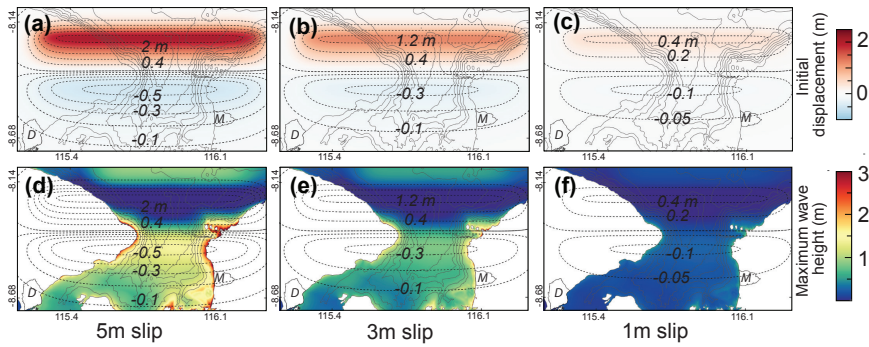
Deleted: The first wave arrives at ~10-15 minutes and reaches its peak at ~30 minutes. It is followed by a drawdown at ~40 minutes and a second wave at ~45 minutes

Deleted: 1

Deleted: For model A, the maximum wave height generated is ~1.1-1.3 m for 5 m slip, ~0.7-0.8 m for 3 m slip, and ~0.3 m for 1 m slip. For model B, the maximum wave height is ~0.7-1.1 m for 5 m slip, ~0.4-0.7 m for 3 m slip and ≤ 0.3 m for 1 m slip

Deleted: results

608



609

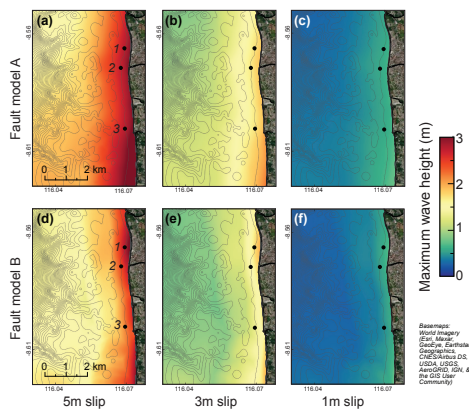
Figure 8: Initial surface deformation and maximum wave heights in 1 hr generated by different slip amounts on the upper half of the fault ramp (model B). Upper panels (a-c): The coseismic deformation generated by (a) 5 m, (b) 3 m, and (c) 1 m fault slip events result in a narrow uplift patch in the north and broader subsidence in the south. Lower panels (d-f): Maximum sea surface displacements for (d) 5 m, (e) 3 m, and (f) 1 m fault slip events. Maps are adjusted to show wave heights relative to the post-earthquake land surface rather than initial sea level by subtracting the coseismic displacement (dashed contour lines). The highest waves are concentrated around the headlands of Lombok and Bali at 8.38°S and the mid-west coast of Lombok. Polygons on land – cities of Denpasar, Bali and Mataram, Lombok. D = Denpasar, M = Mataram.

Deleted: results

610

611

612



613

Figure 9: Maximum wave heights in Mataram, based on simulations in grid layer 2 (L2, Fig. 6), generated by slip on fault models A (a-c) and B (d-f). Models A-5 (a) and B-5 (d) generate wave heights of ~2.5 to 2.7 m; Models A-3 (b) and

Deleted: The 5 m slip models

Deleted: a,d

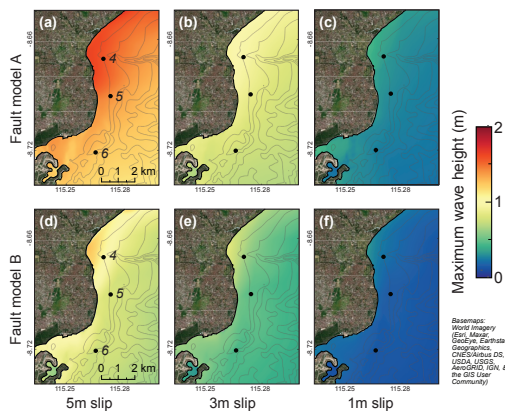
Deleted: 3.3

Deleted: the 3 m slip models (b,e)

B-3 (e) generate ~1.6 to 1.7 m high waves; the models A-1 (c) and B-1 (f) generate ≤ 0.6 m high waves. Basemaps – World Imagery. Dots – tide gauges.

614
615
616

- Deleted: 5
- Deleted: 2.1
- Deleted: 1 m slip models
- Deleted: (c,f)
- Deleted: ~
- Deleted: to 0.7

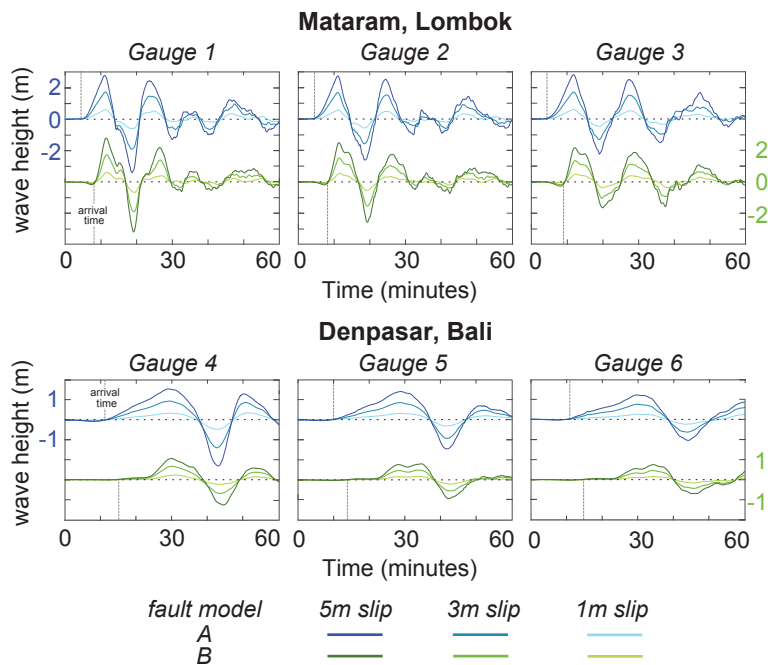


617

Figure 10: Maximum wave heights in Denpasar generated by slip on fault models A (a-c) and B (d-f). The highest tsunami wave heights are located within the semi-enclosed bay on the northeast coast. The maximum wave height near Denpasar range is ~1.4 m for model A-5 (a), ~0.9 m for A-3 (b), and ~0.3 m for A-1 (c). The maximum wave heights are slightly lower in fault model B. It is ~0.8 m for model B-5 (d), ~0.6 m for B-3 (e), and ≤ 0.2 m for B-1 (f). Basemaps – World Imagery. Dots – tide gauges.

618

- Deleted: s
- Deleted: for model A
- Deleted: from
- Deleted: 1
- Deleted: to 1.5 m
- Deleted: for 5 m slip (a),
- Deleted: 7 to 1.1
- Deleted: 3 m slip
- Deleted: 3 to 0.4
- Deleted: 1 m slip
- Deleted: For
- Deleted: , the maximum wave heights are
- Deleted: 7 to 1.2
- Deleted: 5 m slip
- Deleted: .4 to 0.8
- Deleted: 3 m slip
- Deleted: ~
- Deleted: to 0.3
- Deleted: for 1 m slip



619

620 Figure 11: Sea surface elevation generated by fault models A and B recorded at virtual tide gauges located along the
 621 10 m water depth contours offshore Mataram (gauges 1 to 3) and Denpasar (gauges 4 to 6). The records for fault models
 622 A and B in Mataram are similar in terms of wave heights and arrival times. In Denpasar, the models have similar wave
 623 patterns but the arrival times for model A is slightly earlier than in model B. After the earthquake, the first tsunami in
 624 Mataram arrives at 9 minutes, while in Denpasar it arrives at 1218 minutes for model A and 2327 minutes. The
 625 peak of the first wave is at ~11 minutes and ~30 minutes in Mataram and Denpasar, respectively.

626

627 3.3 Inundation in Mataram, Lombok

628 Tsunami waves of a given height at the coastline can have variable impact depending on the topography and
 629 infrastructure on land. Because inundation modeling requires a detailed Digital Surface Model for accurate results
 630 and significant computational time, we limit the inundation modeling to the city of Mataram, Lombok, because
 631 this region is densely populated (Fig. 6) and is exposed to the highest waves in our tsunami models. We run the
 632 modeling for fault model A-5 to represent the inundation of the worst-case earthquake scenario used in this study.

633

634 Based on our results, 5 m of fault slip generates two >2 m high waves followed by two lower waves that hit the
 635 coast at Mataram city (Fig. 11). These waves inundate Mataram with flow depths of generally 2 m but can reach
 636 as high as 3 m on the southern coast (Figs. 12 and 13). The extent of inundation is ~55-140 m along the northern
 637 to the middle parts of the coast; in the south, it reaches ~230 m. This much wider extent in the south correlates
 638 with a lower density of structures. We interpret that the presence of closely packed structures in the north limits
 639 the inundation further inland. Our results are based on the model assumption that these structures can withstand

Deleted: the arrival

Deleted: are similar for both models, but the wave heights are higher for model A.

Deleted: 8

Deleted: 0

Deleted: 15

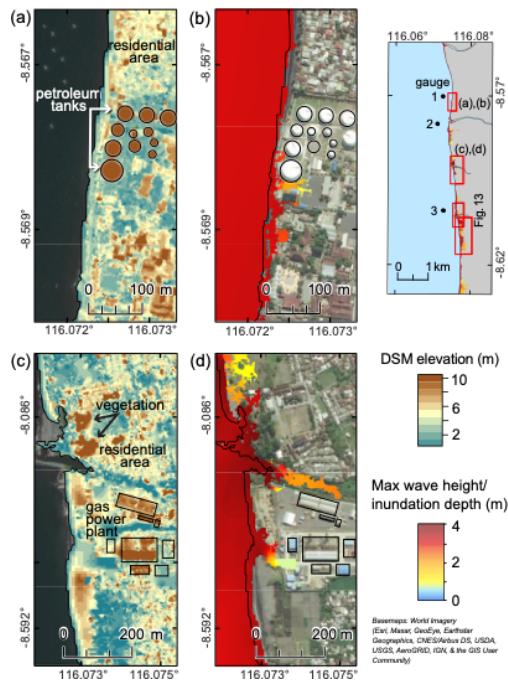
Formatted: Font: 9 pt, Bold

Deleted: the highest value of fault slip (5 m) for fault model A (full rupture)

Deleted: our

Deleted: 1.5

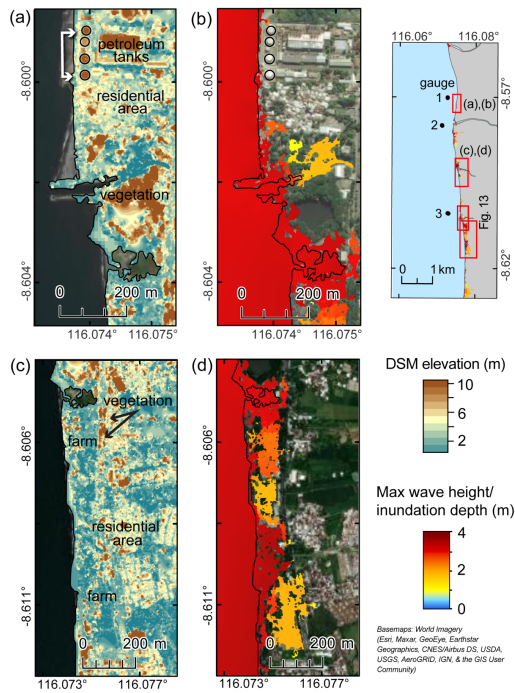
650 the flow; in a real tsunami event, some structures could be destroyed (e.g., 2011 Tohoku earthquake and tsunami,
 651 Mori et al., 2013), which could reduce flow resistance and increase the inundation distance.
 652
 653 The inundation has limited extent where the beach is narrow and there are dense structures near the coast. For
 654 instance, along the northern (Figs. 12a-b) and mid-southern coasts (Figs 13a-b), inundation is limited to within
 655 the ~15-20 m wide beach, and the closely packed residential structures just behind the beach are not inundated.
 656 At industrial sites where there are more open spaces (Figs. 12a-b and 13a-b), the inundation extent can reach to
 657 ~95-140 m (Figs. 12a-d). When the beach is wider and the structures are further from the coast, the inundation
 658 extends further inland (Figs. 12c-d and 13c-d). We note that in our model, clustered vegetation on the beach is
 659 represented in the DSM as a solid barrier, and thus is able to entirely block the flow (upper part of Fig. 12c-d). In
 660 reality, clustered vegetation can slow but not completely obstruct the flow; the inundation extent at this site is
 661 therefore likely underestimated. Using a digital terrain model, on the other hand, would overestimate the
 662 inundation extent (Muhari et al., 2011). Our results may be more realistic in regions where vegetation is absent,
 663 as in the lower part of Fig. 13a-b, where we model ~175 m inundation. Along the southern coast, the beach is
 664 generally 20-40 m wide and most of the area is farmland; with more open space, the inundation is able to reach
 665 ~230 m inland (Figs. 13c-d).
 666
 667



668
 Figure 12: The DSM elevation and inundation on the northern coast of Mataram associated with 5 m of coseismic slip on the Flores thrust ramp (model A-5) overlain on World Imagery. Flow depth is generally ≤ 1.5 m. (a-b) The inundation

extent is limited by the high density of structures in residential areas. The inundation reaches ~95 m at the industrial site (circular features are petroleum tanks), where there are more open spaces. (c-d) Inundation may be underestimated in regions where vegetation clusters act in the model as wide barriers to flow but may be more porous, as shown in the upper half of the map. In the area of the gas power plant, where there is less vegetation and the structures are more widely spaced, the inundation extent is ~140 m. Right image – location map of figures.

669



670

671 **Figure 13:** The DSM elevation and inundation on the southern coast of Mataram associated with 5 m of coseismic slip
 672 on the Flores thrust ramp (model A-5) overlain on World Imagery. (a-b) To the south of the industrial site (with
 673 petroleum tanks), the inundation depth is ≤ 1.5 m and the inundation extent is ~175 m. (c-d) In the south, inundation is
 674 more extensive, likely because of the lower density of structures and wider open area (beach and farmland). The
 675 inundation depth is generally 2-3m and the extent reaches to ~230 m. Right image – location map of figures.

676

677 4 Conclusions

678 The Flores Thrust is an active south-dipping back-arc fault system traversing north of the Lesser Sunda Islands.
 679 The 2018 Lombok earthquake sequence and prior historical events show that the western part of the fault zone is
 680 capable of generating tsunamigenic earthquakes. In this work, we study the tsunami potential associated with
 681 coseismic slip on the blind fault ramp below Lombok Strait, located between the islands of Lombok and Bali,
 682 [using deterministic tsunami modelling](#). We focus on the tsunami patterns near the capital cities of Mataram,
 683 Lombok and Denpasar, Bali, which both lie on the coasts facing the strait. Our modeling is based on a geologically
 684 constrained model of the fault, informed by the 2018 earthquake sequence. Tsunami propagation is modeled using

685 a high-resolution bathymetry dataset generated by combining data points from the global GEBCO dataset with
686 sounding data digitized from the official nautical charts of Indonesia, interpolated using the Topo to Raster tool
687 in ArcGIS.

688

689 Our results show that fault rupture in this region with 1-5 m of coseismic slip could trigger a tsunami that would
690 hit Mataram, Lombok in ~~9~~ minutes and Denpasar, Bali in ~~12-18~~ minutes with multiple waves. Furthermore,
691 both cities would experience coseismic subsidence of 20-40 cm, exacerbating their exposure to the tsunami hazard
692 and leading to more long-lasting coastal vulnerability. The maximum wave heights in Mataram are ~~1.6~~ to ~~2.7~~ m
693 for 3-5 m of coseismic slip, while Denpasar has maximum wave heights of ~~0.6~~ to ~~1.4~~ m. Overall, the coast along
694 Mataram city is more prone than Denpasar to high tsunamis arriving quickly.

695

696 Because Mataram experiences higher wave heights, we also modelled the inundation in this region for our worst-
697 case scenario (5 m slip) using a high-resolution DSM. We found that the inundation extends for ~55-140 m inland
698 with a maximum flow depth of ~2-3 m, and, except in the region just south of the city, where the inundation
699 reaches 230 m. This difference in inundation extent appears to be primarily influenced by the structures present
700 near the coast, which are denser in the north. However, if structures are destroyed by flow, inundation could reach
701 further inland.

702

703 Because of the proximity of the Flores thrust ramp to the coasts of Lombok and Bali, associated tsunamis would
704 hit within <15 minutes after the earthquake. This early tsunami arrival would mean little time for evacuation. In
705 the case of the 2018 Lombok earthquake, the residents of northern Lombok started evacuation only after a
706 government announcement, and the evacuation took at least 20 minutes (Tsimopoulou et al., 2020). For a potential
707 tsunami in Mataram caused by slip on the Flores thrust, there is insufficient time to wait for an announcement
708 after the earthquake. Hence, raising community awareness about earthquake-generated tsunamis and evacuation
709 plans is important, so that residents will know to respond immediately after experiencing strong ground shaking.
710 Furthermore, the initial polarity of the waves would be positive, and thus there would be no warning signal from
711 drawdown prior to inundation. In addition, a second high wave would hit Mataram coast at ~20 minutes,
712 emphasizing the need for continued heightened alert following the first inundation.

713

714 We finally note that some of the structures built along the coast are industrial, with several petroleum tanks and a
715 gas power plant. The impacts of natural disasters can be multiplied when natural events trigger industrial events
716 ('Natural Hazards Triggering Technological Disasters,' or Natech) (Cruz and Suarez-Paba, 2019). Tsunamis in
717 particular have a history of causing Natech events (e.g. (Suppasri et al., 2021); for instance, the 2011 Mw9.1
718 Tohoku earthquake and tsunami led to not only meltdown at the Fukushima-Daichi nuclear power plant, but also
719 fires, explosions, and hazardous materials release at industrial sites (Krausmann and Cruz, 2013). In Mataram,
720 damage to the petroleum tanks, power plant, and other industrial equipment by groundshaking or inundation could
721 trigger Natech events, including fires, explosions, and pollution of the coastal water and associated ecological
722 damage. Evaluating these sites to understand and strengthen their resilience to these hazards should be a priority.

723

Deleted: ~11

Deleted: 30

Deleted: 5

Deleted: 3.3

Deleted: 7

Deleted: 5

730 While most tsunami modeling studies in Indonesia have focused on the hazard associated with large tsunamis
731 triggered by megathrust ruptures, such as the devastating 2004 Indian Ocean earthquake and tsunami (e.g. Wang
732 and Liu, 2007), we highlight here the hazard associated with smaller, local events caused by slip on a back-arc
733 thrust system. One of the challenges with local studies is the need for detailed and accurate fault models and
734 bathymetry datasets. We show that geological information such as regional and nearby seismicity can be combined
735 with bathymetry, topography, and seismic reflection data to model fault geometry, and that a high-resolution
736 bathymetry dataset can be generated by combining globally available bathymetric data with sounding
737 measurements collected for navigation purposes. Specifically, for earthquake-triggered tsunamis in Indonesia, the
738 official nautical charts for Indonesia provide dense measurements offshore shallow coastal cities. Integrating these
739 datasets can provide more accurate forecasts and hazard estimations for both tsunami wave height and arrival
740 time, for local and regional studies, and could be replicated for other fault systems and areas.

741

742 **DATA AVAILABILITY**

743 The animation of the tsunami propagation for the 5 m coseismic slip on the full fault ramp can be accessed at

744 <https://researchdata.ntu.edu.sg/privateurl.xhtml?token=ed262ac9-0649-4d39-9c34-104c0e93f6f1>,

745 The inundation model for Mataram, Lombok can be accessed at

746 <https://researchdata.ntu.edu.sg/privateurl.xhtml?token=0b2a3b5b-2731-4394-8442-fa5b24a04642>

747

748 **AUTHOR CONTRIBUTION**

749 RPF, JAH and KEB conceptualized the research. RPF conducted the modeling and the formal analysis. JAH and
750 KEB acquired the funding. JAH supervised the overall work. JAH, KEB and KLH assisted with the fault model
751 setup. LL and ADS assisted with the tsunami modelling. RPF generated the figures. RPF and JAH wrote the
752 original draft. JAH, KEB, KHL, LL and ADS reviewed and edited the manuscript.

753

754 **COMPETING INTERESTS**

755 The authors declare no competing interests.

756

757 **ACKNOWLEDGMENTS**

758 The maps in this paper were made using ArcGIS® software by Esri. The World Ocean Base map is attributed to
759 Esri, GEBCO, NOAA, Garmin, HERE, and other contributors. The World Imagery basemap is attributed to Esri,
760 Maxar, Earthstar Geographics, USDA FSA, USGS, Aerogrid, IGN, IGP, and the GIS User Community. The
761 ArcGIS® and ArcMap™ are the intellectual property of Esri and are used herein under license. Copyright © Esri.
762 All rights reserved. We would like to thank Rishav Mallick for helping in creating figure 4 using the Unicycle
763 code (Moore et al., 2019).

764

765 This research was supported by the Earth Observatory of Singapore via its funding from the National Research
766 Foundation Singapore and the Singapore Ministry of Education under the Research Centres of Excellence
767 initiative. This work comprises EOS contribution number 408. The project was also supported by National Natural
768 Science Foundation China (No 41976197).

769

Deleted: <https://researchdata.ntu.edu.sg/privateurl.xhtml?token=ed262ac9-0649-4d39-9c34-104c0e93f6f1>

772

773 **REFERENCES**

774

- 775 Afif, H., and A. Cipta, 2015, Tsunami hazard map in eastern Bali, AIP Conf. Proc., 1658, no. April, doi:
776 10.1063/1.4915041.
- 777 Ammon, C. J., H. Kanamori, and T. Lay, 2008, A great earthquake doublet and seismic stress transfer cycle in
778 the central Kuril islands, *Nature*, 451, no. 7178, 561–565, doi: 10.1038/nature06521.
- 779 Beckers, J., and T. Lay, 1995, Very broadband seismic analysis of the 1992 Flores, Indonesia, earthquake (Mw
780 = 7.9), *J. Geophys. Res.*, 100, no. B9, doi: 10.1029/95jb01689.
- 781 Van Bemmelen, R. W., 1949, General Geology of Indonesia and adjacent archipelagoes, *Geol. Indones.*
- 782 Bilek, S. L., 2010, Invited review paper: Seismicity along the South American subduction zone: Review of large
783 earthquakes, tsunamis, and subduction zone complexity, *Tectonophysics*, 495, nos. 1–2, 2–14, doi:
784 10.1016/j.tecto.2009.02.037.
- 785 Boekschoten, G. J., M. B. Best, and K. S. Putra, 2000, Balinese reefs in historical context, in *Proceedings 9th*
786 *International Coral Reef Symposium*, Citeseer, 23–27.
- 787 Bondarenko, M., D. Kerr, A. Sorichetta, and A. Tatem, 2020, Census/projection-disaggregated gridded
788 population datasets for 189 countries in 2020 using Built-Settlement Growth Model (BSGM) outputs, doi:
789 10.5258/SOTON/WP00684.
- 790 Bowin, C., G. M. Purdy, C. Johnston, G. Shor, H. M. S. Lawver, L. Hartono, and P. Jezek, 1980, Arc-Continent
791 Collision in Banda Sea Region, *Am. Assoc. Pet. Geol. Bull.*, 64, doi: 10.1306/2F9193CD-16CE-11D7-
792 8645000102C1865D.
- 793 Chau, K. T., and K. T. S. Lam, 2015, Field observations and numerical simulations of the 2011 Tohoku tsunami
794 using COMCOT, *Comput. Methods Recent Adv. Geomech. - Proc. 14th Int. Conf. Int. Assoc. Comput.*
795 *Methods Recent Adv. Geomech. IACMAG 2014*, 1841–1846, doi: 10.1201/b17435-326.
- 796 Cruz, A. M., and M. C. Suarez-Paba, 2019, Advances in Natech research: An overview, *Prog. Disaster Sci.*, 1,
797 100013, doi: 10.1016/j.pdisas.2019.100013.
- 798 Darmawan, H. et al., 2020, Topography and structural changes of Anak Krakatau due to the December 2018
799 catastrophic events, *Indones. J. Geogr.*, 52, no. 3, 402, doi: 10.22146/ijg.53740.
- 800 Dewey, J. F., and J. M. Bird, 1970, Mountain belts and the new global tectonics, *J. Geophys. Res.*, 75, no. 14,
801 2625–2647, doi: 10.1029/JB075i014p02625.
- 802 Felix, R. P., J. A. Hubbard, J. D. P. Moore, and A. D. Switzer, 2021, The Role of Frontal Thrusts in Tsunami
803 Earthquake Generation, *Bull. Seismol. Soc. Am.*, doi: 10.1785/0120210154.
- 804 Fraser, S. A., W. L. Power, X. Wang, L. M. Wallace, C. Mueller, and D. M. Johnston, 2014, Tsunami
805 inundation in Napier, New Zealand, due to local earthquake sources, *Nat. Hazards*, 70, no. 1, 415–445,
806 doi: 10.1007/s11069-013-0820-x.
- 807 Griffin, J. et al., 2015, An evaluation of onshore digital elevation models for modeling tsunami inundation
808 zones, *Front. Earth Sci.*, 3, doi: 10.3389/feart.2015.00032.
- 809 Griffin, J., N. Nguyen, P. Cummins, and A. Cipta, 2019, Historical earthquakes of the eastern sunda arc: Source
810 mechanisms and intensity-based testing of Indonesia’s national seismic hazard assessment, *Bull. Seismol.*
811 *Soc. Am.*, 109, no. 1, 43–65, doi: 10.1785/0120180085.

812 Hall, R., and W. Spakman, 2015, Mantle structure and tectonic history of SE Asia, *Tectonophysics*, 658, 14–45,
813 doi: 10.1016/j.tecto.2015.07.003.

814 Hamilton, W., 1979, *Tectonics of the Indonesian region*, US Government Printing Office.

815 Hamzah, L., N. Puspito, and F. Imamura, 2000, *Tsunami Catalog Indonesia.pdf*, 25–43.

816 Hill, E. M. et al., 2012, The 2010 Mw 7.8 Mentawai earthquake: Very shallow source of a rare tsunami
817 earthquake determined from tsunami field survey and near-field GPS data, *J. Geophys. Res. Solid Earth*,
818 117, no. 6, doi: 10.1029/2012JB009159.

819 Horspool, N., I. Pranantyo, J. Griffin, H. Latief, D. H. Natawidjaja, W. Kongko, A. Cipta, B. Bustaman, S. D.
820 Anugrah, and H. K. Thio, 2014, A probabilistic tsunami hazard assessment for Indonesia, *Nat. Hazards*
821 *Earth Syst. Sci.*, 14, no. 11, 3105–3122, doi: 10.5194/nhess-14-3105-2014.

822 Hutchinson, M. F., 1989, A new procedure for gridding elevation and stream line data with automatic removal
823 of spurious pits, *J. Hydrol.*, 106, nos. 3–4, 211–232, doi: 10.1016/0022-1694(89)90073-5.

824 Imamura, F., and M. Kikuchi, 1994, Moment release of the 1992 Flores Island earthquake inferred from tsunami
825 and teleseismic data, *Sci. Tsunami Hazards*, 12, 67–76.

826 Kaiser, G., L. Scheele, A. Kortenhaus, F. Løvholt, H. Römer, and S. Leschka, 2011, The influence of land cover
827 roughness on the results of high resolution tsunami inundation modeling, *Nat. Hazards Earth Syst. Sci.*,
828 11, no. 9, 2521–2540, doi: 10.5194/nhess-11-2521-2011.

829 Kajjura, K., 1963, The Leading Edge of a Tsunami, *Bull. Earthq. Res. Inst.*, 41, 535–571.

830 Kardoso, R., and A. A. C. Dewi, 2021, Tsunami inundation maps in Mataram City based on tsunami modeling,
831 in *Proceeding International Conference on Science (ICST)*, 273–278.

832 Koulali, A., S. Susilo, S. McClusky, I. Meilano, P. Cummins, P. Tregoning, G. Lister, J. Efendi, and M. A.
833 Syafi'i, 2016, Crustal strain partitioning and the associated earthquake hazard in the eastern Sunda-Banda
834 Arc, *Geophys. Res. Lett.*, 43, no. 5, 1943–1949, doi: 10.1002/2016GL067941.

835 Krausmann, E., and A. M. Cruz, 2013, Impact of the 11 March 2011, Great East Japan earthquake and tsunami
836 on the chemical industry, *Nat. Hazards*, 67, no. 2, 811–828, doi: 10.1007/s11069-013-0607-0.

837 Kulikov, E. A., V. K. Gusiakov, A. A. Ivanova, and B. V. Baranov, 2016, Numerical tsunami modeling and the
838 bottom relief, *Moscow Univ. Phys. Bull.*, 71, no. 6, 527–536, doi: 10.3103/S002713491605012X.

839 Kurniawan, T., and A. F. Laili, 2019, Penentuan Area Terdampak "Ketinggian Maksimum Tsunami" di Pulau
840 Bali Berdasarkan Potensi Gempabumi Pembangkit Tsunami Pada Segmen Megathrust Sumba, *J. Dialog*
841 *dan Penanggulangan Bencana*, 10, no. 1, 93–104.

842 Liu, Philip L.F., Y. S. Cho, M. J. Briggs, U. Kanoglu, and C. E. Synolakis, 1995, Runup of solitary waves on a
843 circular Island, *J. Fluid Mech.*, 302, no. 37, 259–285, doi: 10.1017/S0022112095004095.

844 Liu, P.L.F., Y. S. Cho, S. B. Yoon, and S. N. Seo, 1995, Numerical Simulations of the 1960 Chilean Tsunami
845 Propagation and Inundation at Hilo, Hawaii, 99–115.

846 Løvholt, F., D. Kühn, H. Bungum, C. B. Harbitz, and S. Glimsdal, 2012, Historical tsunamis and present
847 tsunami hazard in eastern Indonesia and the southern Philippines, *J. Geophys. Res. Solid Earth*, 117, no.
848 B9, doi: 10.1029/2012JB009425.

849 Lythgoe, K., M. Muzli, K. Bradley, T. Wang, A. D. Nugraha, Z. Zulfakriza, S. Widiyantoro, and S. Wei, 2021,
850 Thermal squeezing of the seismogenic zone controlled rupture of the volcano-rooted Flores Thrust, *Sci.*
851 *Adv.*, 7, no. 5, 1–9, doi: 10.1126/SCIADV.ABE2348.

852 Marks, K. M., and W. H. F. Smith, 2006, An Evaluation of Publicly Available Global Bathymetry Grids, *Mar.*
853 *Geophys. Res.*, 27, no. 1, 19–34, doi: 10.1007/s11001-005-2095-4.

854 McCaffrey, R., and J. Nabelek, 1987, Earthquakes, gravity, and the origin of the Bali Basin: An example of a
855 Nascent Continental Fold-and-Thrust Belt, *J. Geophys. Res.*, 92, no. B1, 441, doi:
856 10.1029/JB092iB01p00441.

857 Moore, J. D. P., S. Barbot, E. Lindsey, S. Masuti, and J. Muto, 2019, jdpmoore/unicycle: Unicycle, doi:
858 10.5281/ZENODO.4471162.

859 Muhari, A., F. Imamura, S. Koshimura, and J. Post, 2011, Examination of three practical run-up models for
860 assessing tsunami impact on highly populated areas, *Nat. Hazards Earth Syst. Sci.*, 11, no. 12, 3107–3123,
861 doi: 10.5194/nhess-11-3107-2011.

862 Musson, R. M. W., 2012, A provisional catalogue of historical earthquakes in Indonesia, *Br. Geol. Surv.*

863 Nguyen, N., J. Griffin, A. Cipta, and P. R. Cummins, 2015, Indonesia’s Historical Earthquakes: Modelled
864 examples for improving the national hazard map.

865 NOAA, 2021, National Geophysical Data Center / World Data Service: NCEI/WDS Global Historical Tsunami
866 Database. NOAA National Centers for Environmental Information. doi:10.7289/V5PN93H7.

867 Okada, Y., 1992, Internal deformation due to shear and tensile faults in a half-space, *Bull. Seismol. Soc. Am.*,
868 82, no. 2, 1018–1040.

869 Okal, E. A., and J. C. Borrero, 2011, The “tsunami earthquake” of 1932 June 22 in Manzanillo, Mexico:
870 Seismological study and tsunami simulations, *Geophys. J. Int.*, 187, no. 3, 1443–1459, doi:
871 10.1111/j.1365-246X.2011.05199.x.

872 Pradjoko, E., L. Wardani, H. Wardani, H. Sulistiyono, and S. Sulistiyono, 2018, The prediction of tsunami
873 travel time to Mataram City Indonesia based on North Lombok earthquake as the initial condition,
874 MATEC Web Conf., 229, 4–8, doi: 10.1051/mateconf/201822904007.

875 Pranantyo, I. R., M. Heidarzadeh, and P. R. Cummins, 2021, Complex tsunami hazards in eastern Indonesia
876 from seismic and non-seismic sources: Deterministic modelling based on historical and modern data,
877 *Geosci. Lett.*, 8, no. 1, 20, doi: 10.1186/s40562-021-00190-y.

878 Rakowsky, N., A. Androsov, A. Fuchs, S. Harig, A. Immerz, S. Danilov, W. Hiller, and J. Schröter, 2013,
879 Operational tsunami modelling with TsunAWI - Recent developments and applications, *Nat. Hazards*
880 *Earth Syst. Sci.*, 13, no. 6, 1629–1642, doi: 10.5194/nhess-13-1629-2013.

881 Rastogi, B. K., and R. K. Jaiswal, 2006, A Catalog of Tsunamis in the Indian Ocean, *Sci. Tsunami Hazards*, 25,
882 no. 3, 128–143.

883 Regnier, M., S. Calmant, B. Pelletier, Y. Lagabrielle, and G. Cabioch, 2003, The M w 7.5 1999 Ambrym
884 earthquake, Vanuatu: A back arc intraplate thrust event, *Tectonics*, 22, no. 4, n/a-n/a, doi:
885 10.1029/2002TC001422.

886 Rusli, Irjan, and A. Rudyanto, 2012, Pemodelan Tsunami Sebagai Bahan Mitigasi Bencana Studi Kasus
887 Sumenep Dan Kepulauannya, *J. Neutrino*, doi: 10.18860/neu.v0i0.1639.

888 Salaree, A., Y. Huang, M. D. Ramos, and S. Stein, 2021, Relative Tsunami Hazard From Segments of Cascadia
889 Subduction Zone For Mw 7.5–9.2 Earthquakes, *Geophys. Res. Lett.*, 48, no. 16, 1–10, doi:
890 10.1029/2021GL094174.

891 Sallarès, V., M. Prada, S. Riquelme, A. Meléndez, A. Calahorrano, I. Grevemeyer, and C. R. Ranero, 2021,

892 Large slip, long duration, and moderate shaking of the Nicaragua 1992 tsunami earthquake caused by low
893 near-trench rock rigidity, *Sci. Adv.*, 7, no. 32, doi: 10.1126/sciadv.abg8659.

894 Sallarès, V., and C. R. Ranero, 2019, Upper-plate rigidity determines depth-varying rupture behaviour of
895 megathrust earthquakes, *Nature*, 576, no. 7785, 96–101, doi: 10.1038/s41586-019-1784-0.

896 Salman, R. et al., 2020, Cascading partial rupture of the flores thrust during the 2018 lombok earthquake
897 sequence, indonesia, *Seismol. Res. Lett.*, 91, no. 4, 2141–2151, doi: 10.1785/0220190378.

898 Satake, K., 1988, Effects of bathymetry on tsunami propagation: Application of ray tracing to tsunamis, *Pure
899 Appl. Geophys.* PAGEOPH, 126, no. 1, 27–36, doi: 10.1007/BF00876912.

900 Satake, K., 1995, Linear and nonlinear computations of the 1992 Nicaragua earthquake tsunami, *Pure Appl.
901 Geophys.*, 144, nos. 3–4, 455–470, doi: 10.1007/BF00874378.

902 Serra, C. S. et al., 2021, Sensitivity of Tsunami Scenarios to Complex Fault Geometry and Heterogeneous Slip
903 Distribution: Case-Studies for SW Iberia and NW Morocco, *J. Geophys. Res. Solid Earth*, 126, no. 10, 1–
904 19, doi: 10.1029/2021JB022127.

905 Silver, E. A., N. A. Breen, H. Prasetyo, and D. M. Hussong, 1986, Multibeam study of the Flores Backarc
906 Thrust Belt, Indonesia, *J. Geophys. Res. Solid Earth*, 91, no. B3, 3489–3500, doi:
907 10.1029/JB091iB03p03489.

908 Silver, E. A., and D. L. Reed, 1988, Backthrusting in accretionary prism, *J. Geophys. Res.*, 93, no. B4, 3116–
909 3126.

910 Silver, E. A., D. Reed, R. McCaffrey, and Y. Joyodiwiryono, 1983, Back arc thrusting in the Eastern Sunda Arc,
911 Indonesia: A consequence of arc-continent collision, *J. Geophys. Res. Solid Earth*, 88, no. B9, 7429–7448,
912 doi: 10.1029/JB088iB09p07429.

913 Suardana, A. A. M. A. P., D. N. Sugianto, and M. Helmi, 2019, Study of Characteristics and the Coverage of
914 Tsunami Wave Using 2D Numerical Modeling in the South Coast of Bali, Indonesia, *Indones. J. Ocean.
915 Geogr.*, 13, 237–250.

916 Suárez, G., M. Pardo, J. Domínguez, L. Ponce, W. Montero, I. Boschini, and W. Rojas, 1995, The Limón, Costa
917 Rica earthquake of April 22, 1991: Back arc thrusting and collisional tectonics in a subduction
918 environment, *Tectonics*, 14, no. 2, 518–530, doi: 10.1029/94TC02546.

919 Sulaeman, H., 2018, Discovery of Paleotsunami Deposits along Eastern Sunda Arc: Potential for Megathrust
920 Earthquakes in Bali, Brigham Young University.

921 Suppasri, A., E. Maly, M. Kitamura, Syamsidik, G. Pescaroli, D. Alexander, and F. Imamura, 2021, Cascading
922 disasters triggered by tsunami hazards: A perspective for critical infrastructure resilience and disaster risk
923 reduction, *Int. J. Disaster Risk Reduct.*, 66, 102597, doi: 10.1016/j.ijdr.2021.102597.

924 Thingbaijam, K. K. S., P. M. Mai, and K. Goda, 2017, New empirical earthquake source-scaling laws, *Bull.
925 Seismol. Soc. Am.*, 107, no. 5, 2225–2246, doi: 10.1785/0120170017.

926 Tri Laksono, F. A., M. R. Aditama, R. Setijadi, and G. Ramadhan, 2020, Run-up Height and Flow Depth
927 Simulation of the 2006 South Java Tsunami Using COMCOT on Widarapayung Beach, *IOP Conf. Ser.
928 Mater. Sci. Eng.*, 982, 012047, doi: 10.1088/1757-899X/982/1/012047.

929 Tsimopoulou, V., T. Mikami, T. T. Hossain, H. Takagi, M. Esteban, and N. A. Utama, 2020, Uncovering
930 unnoticed small-scale tsunamis: field survey in Lombok, Indonesia, following the 2018 earthquakes, *Nat.
931 Hazards*, 103, no. 2, 2045–2070, doi: 10.1007/s11069-020-04071-z.

932 Tsuji, Y., H. Matsutomi, F. Imamura, M. Takeo, Y. Kawata, M. Matsuyama, T. Takahashi, Sunarjo, and P.
933 Harjadi, 1995, Damage to coastal villages due to the 1992 Flores Island earthquake tsunami, *Pure Appl.*
934 *Geophys. PAGEOPH*, 144, nos. 3–4, 481–524, doi: 10.1007/BF00874380.

935 Wang, X., and P. L.-F. Liu, 2007, Numerical Simulations of the 2004 Indian Ocean Tsunamis — Coastal
936 Effects, *J. Earthq. Tsunami*, 01, no. 03, 273–297, doi: 10.1142/s179343110700016x.

937 Wang, X., and W. Power, 2011, COMCOT: a Tsunami Generation Propagation and Run-up Model.

938 Wibowo, S. B., D. S. Hadmoko, Y. Isnaeni, N. M. Farda, A. F. S. Putri, I. W. Nurani, and S. H. Supangkat,
939 2021, Spatio-Temporal Distribution of Ground Deformation Due to 2018 Lombok Earthquake Series,
940 *Remote Sens.*, 13, no. 11, 2222, doi: 10.3390/rs13112222.

941 Wibowo, M., W. Kongko, W. Hendriyono, and S. Karima, 2021, Tsunami Hazard Potential Modeling as
942 Tourism Development Considerations in the North of Lombok Strait, *IOP Conf. Ser. Earth Environ. Sci.*,
943 832, no. 1, 012047, doi: 10.1088/1755-1315/832/1/012047.

944 Wilson, K. M., and H. E. Power, 2020, Tsunami Modelling with Static and Dynamic Tides in Drowned River
945 Valleys with Morphological Constrictions, *Pure Appl. Geophys.*, 177, no. 3, 1595–1616, doi:
946 10.1007/s00024-019-02411-0.

947 Yang, X., S. C. Singh, and A. Tripathi, 2020, Did the Flores backarc thrust rupture offshore during the 2018
948 Lombok earthquake sequence in Indonesia?, *Geophys. J. Int.*, 221, no. 2, 758–768, doi:
949 10.1093/gji/ggaa018.

950 Yeh, H., F. Imamura, C. Synolakis, Y. Tsuji, P. Liu, and S. Shi, 1993, The Flores Island tsunamis, *Eos, Trans.*
951 *Am. Geophys. Union*, 74, no. 33, 369–373, doi: 10.1029/93EO00381.

952